

A Study of Radio Polarization in Protostellar Jets

Mariana Cécere^{1,5}, Pablo F. Velázquez², Anabella T. Araudo³, Fabio De Colle²,
Alejandro Esquivel², Carlos Carrasco-González⁴, and Luis F. Rodríguez⁴

ABSTRACT

Synchrotron radiation is commonly observed associated with shocks of different velocities, ranging from relativistic shocks associated with active galactic nuclei, gamma-ray bursts or microquasars to weakly- or non-relativistic flows as those in supernova remnants. Recent observations of synchrotron emission in protostellar jets are important not only because they extend the range over which the acceleration process works, but also because they allow to determine the jet and/or interstellar magnetic field structure, thus giving insights on the jet ejection and collimation mechanisms. In this paper, we compute for the first time polarized (synchrotron) and non polarized (thermal X-ray) synthetic emission maps from axisymmetrical simulations of magnetized protostellar jets. We consider models with different jet velocities and variability, as well as toroidal or helical magnetic field. Our simulations show that variable, low-density jets with velocities $\sim 1000 \text{ km s}^{-1}$ and ~ 10 times lighter than the environment can produce internal knots with significant synchrotron emission, and thermal X-rays in the shocked region of the leading bow shock moving in a dense medium. In addition, models with helical magnetic fields show, in agreement with observations of protostellar jets, a decrease in the degree of polarization of synchrotron emission towards the jet axis, which is not observed in models with a purely toroidal magnetic field.

Subject headings: Herbig-Haro objects — ISM: jets and outflows — magnetohydrodynamics (MHD) — polarization — radiation mechanisms: non-thermal — shock waves

1. Introduction

Jets are present in astrophysical sources with various spatial scales, from Young Stellar Objects (YSOs) to active galactic nuclei. These collimated outflows are generally considered to be the result of bipolar ejection of plasma, associated with accretion onto a central object

(Blandford & Payne 1982). Variability in the ejection speed can produce internal shocks clearly seen in YSO jets in the form of bright optical knots (e.g., Raga & Noriega-Crespo 1998; Masciadri et al. 2002) called Herbig-Haro (HH) objects.

Jets that arise from active galaxies can have relativistic speeds, and are well known synchrotron radiation emitters (see for example Tregillis et al. 2001; Laing et al. 2006; Gómez et al. 2008). In contrast, YSO jets are non-relativistic and typically thermal radio sources. However, a few stellar sources, such as Serpens (Rodríguez et al. 1989), HH 80-81 (Marti et al. 1995), Cepheus-A (Garay et al. 1996), W3(OH) (Wilner et al. 1999), and IRAS 16547-4247 (Garay et al. 2003) present radio emission with negative spectral index interpreted as non-thermal (synchrotron) radiation. Notably, polarized radio emission was detected

¹Instituto de Astronomía Teórica y Experimental, Universidad Nacional de Córdoba, X5000BGR, Córdoba, Argentina

²Instituto de Ciencias Nucleares, Universidad Nacional Autónoma de México, Apdo. Postal 70-543, CP: 04510, D.F., México

³University of Oxford, Astrophysics, Keble Road, Oxford OX1 3RH, UK

⁴Instituto de Radioastronomía y Astrofísica, Universidad Nacional Autónoma de México, Apdo. Postal 3-72, 58090, Morelia, Michoacán, México

⁵Consejo Nacional de Investigaciones Científicas y Técnicas (CONICET), Argentina.

in the jet of HH 80-81 (Carrasco-González et al. 2010). Therefore, an interesting question to answer is how jets with velocities of several hundreds km s⁻¹ moving into a dense medium are able to produce shocks where particles can be accelerated up to relativistic energies and produce synchrotron radio emission.

We present a polarization study in order to shed light on the understanding of the non-thermal emission in protostellar jets. We model, by using axisymmetric, magnetohydrodynamic (MHD) simulations, the synchrotron emission, and we compute the resulting polarization map. The paper is organized as follows: in Section 2, we describe the model and the numerical setup; in Section 3 we show the results (synthetic radio, polarization, and X-ray emission maps); and in Section 4 we present our conclusions.

2. Numerical calculations

2.1. Initial setup

Our study is based on 2.5D axisymmetric, MHD simulations carried out with the adaptive mesh refinement, eulerian code *Mezcal* (De Colle & Raga 2006; De Colle et al. 2008, 2012). We consider a 2D axisymmetrical adaptive grid, with a size of 0.2 and 0.5 pc along the r - and z -directions, respectively, and a maximum spatial resolution of 1.56×10^{-4} pc, corresponding to 1280×3200 cells (at the maximum resolution) along the r - and z -directions, and 6 levels of refinement. The environment in which the jet propagates is homogeneous, with a uniform density $n_{\text{env}} = 3000 \text{ cm}^{-3}$, temperature $T_{\text{env}} = 100 \text{ K}$, and magnetic field B_0 . The jet is restricted at every time-step in a region of the computational domain with $r < R_{\text{jet}} = 0.03 \text{ pc}$ and $z < 0.003 \text{ pc}$, with density $n_{\text{jet}} = 300 \text{ cm}^{-3}$ and velocity v_{jet} (along the z -axis). The longitudinal magnetic field (imposed on all computational domain) is $B_z = B_0$, and the toroidal component is given by (Lind et al. 1989)

$$B_\phi(r) = \begin{cases} B_m \left(\frac{r}{R_m} \right) & 0 \leq r < R_m; \\ B_m \left(\frac{R_m}{r} \right) & R_m \leq r < R_{\text{jet}}; \\ 0 & r \geq R_{\text{jet}}, \end{cases} \quad (1)$$

where $R_m = 0.02 \text{ pc}$, and B_m is given in Table 1. In models M4 and M5 B_z and B_m are chosen so that $B (= \sqrt{B_z^2 + B_m^2})$ results of the order of

0.1 mG. The jet pressure profile is constructed to ensure total pressure equilibrium at $t = 0$:

$$p(r) = \begin{cases} \frac{B_m^2}{8\pi} \left(\beta_m - \frac{r^2}{R_m^2} \right) & 0 \leq r < R_m; \\ \frac{B_m^2}{8\pi} \left(\beta_m - \frac{R_m^2}{r^2} \right) & R_m \leq r < R_{\text{jet}}; \\ p_{\text{env}} & r \geq R_{\text{jet}}, \end{cases} \quad (2)$$

where $\beta_m = p_{\text{env}}/(B_m^2/8\pi)$ and $p_{\text{env}} = n_{\text{env}}k_B T_{\text{env}}$.

We consider five different initial configurations. Model M1 represents a continuous jet with constant injection velocity $v_{\text{jet}} = v_0$, whereas models M2–M5 have a time dependent injection velocity of the form

$$v_{\text{jet}} = v_0(1 + \Delta v \cos(\omega t)), \quad (3)$$

where $v_0 = 1000 \text{ km s}^{-1}$ is the mean velocity of the flow, and $\omega = 2\pi/\tau$, $\tau = 50 \text{ yr}$ and Δv are the frequency, periodicity, and amplitude of the variability, respectively. The values of Δv , B_z and jet maximum velocity $v_{\text{max}} = v_0(1 + \Delta v)$ for the different models are given in Table 1.

2.2. Synthetic emission maps

2.2.1. Non-thermal radio emission and Stokes parameters

Synchrotron emission in YSO jets is produced by relativistic electrons accelerated in internal and termination shocks (see Section 3.1). In the present study, we assume that there is a population of relativistic electrons, accelerated in the shocks, with a power-law energy distribution $N_e = K E_e^{-p}$, where $p = 2 = 2\alpha + 1$ for the standard spectral index $\alpha = 0.5$ and $K \propto \epsilon v_s^{-b}$, being v_s the shock velocity. As in Bocchino et al. (2011), the exponent b was chosen to be -1.5 , implying that stronger shocks are more efficient injecting particles. The synchrotron specific intensity is obtained as (Ginzburg & Syrovatskii 1965)

$$i(\nu) \propto K B_\perp^{\alpha+1} \nu^{-\alpha}, \quad (4)$$

Table 1: Initial setup

Model	B_z [mG]	B_m [mG]	Δv	v_{max} [km s ⁻¹]
M1	0	0.1	0	1000
M2	0	0.1	0.2	1200
M3	0	0.1	0.4	1400
M4	$0.1/\sqrt{2}$	$0.1/\sqrt{2}$	0.4	1400
M5	$0.1/\sqrt{10}$	$0.3/\sqrt{10}$	0.4	1400

where B_{\perp} is the component of the magnetic field perpendicular to the line of sight (LoS) and $\nu = 5$ GHz is the frequency. In this study, a dependence with the angle between the shock normal and the post-shocked magnetic field is not considered (see for instance [Orlando et al. 2007](#); [Petruk et al. 2009](#); [Schneiter et al. 2015](#) for a discussion of the acceleration mechanisms in supernova remnants).

We compute the Stokes parameters Q_B and U_B as

$$Q_B(\nu) = \int_{\text{LoS}} f_0 i(\nu) \cos [2\phi(s)] ds, \quad (5)$$

$$U_B(\nu) = \int_{\text{LoS}} f_0 i(\nu) \sin [2\phi(s)] ds, \quad (6)$$

(see e.g. [Clarke et al. 1989](#); [Jun & Norman 1996](#)), where ds is measured along the LoS, $\phi(s)$ is the position angle of the local magnetic field on the plane of the sky, and

$$f_0 = \frac{\alpha + 1}{\alpha + 5/3} \quad (7)$$

is the degree of linear polarization. The intensity of the linearly polarized emission is given by

$$I_P(\nu) = \sqrt{Q_B^2(\nu) + U_B^2(\nu)} \quad (8)$$

and the position angle of the magnetic field, averaged along the LoS, is computed as

$$\chi_B = \frac{1}{2} \tan^{-1}(U_B/Q_B). \quad (9)$$

2.2.2. Thermal X-ray emission

We calculated the thermal emission by integrating the free-free emissivity $j_{\nu}(n_e, T)$ along the LoS. In the low density regime, $j_{\nu}(n_e, T) = n_e^2 \phi(T)$, where n_e is the electron density and T is the temperature. We assume that the post-shock medium is fully ionized, i.e. $n_e \sim n_H$, where n_H is the ion density. The function $\phi(T)$ was constructed with the CHIANTI atomic database ([Dere et al. 1998](#)) considering the energy range [0.15-8] keV and assuming solar metallicity.

3. Results

The numerical simulations with the initial conditions summarized in Table 1 were carried out until an integration time of 1500 yr.

3.1. Shocks in protostellar jets

Figure 1 displays the number density stratification and the velocity field. As the jet interacts with the surrounding medium, it forms a double shock structure, where the environment gas is accelerated by a forward shock, and the jet plasma is decelerated by a reverse shock. This structure, as well as the contact discontinuity separating the shocked interstellar material from the shocked jet material, are clearly visible at the head of the jet shown in Figure 1. In all cases, a slow bowshock travels against the surrounding environment with velocities $\sim [200 - 260]$ km s⁻¹.

Internal shocks are present only in the models where $\Delta v \neq 0$. Several jumps in the jet velocity can be observed by tracing a line along the symmetry axis on velocity distributions maps. These jumps velocities reveal the position of the internal shocks and have values in the range [400 – 500] km s⁻¹. By using the Rankine-Hugoniot jump conditions, the internal shocks velocities are of the order of 1000 km s⁻¹. With these velocities and considering that these shocks move in a low density medium, with densities of the order of 200 cm⁻³, the internal shocks are adiabatic¹. Note that in models M3–M5 ($\Delta v = 0.4$) the bow shock is significantly slower (200 km s⁻¹) than in models M1 and M2 (260 km s⁻¹).

Figure 2 displays the magnitude of the magnetic field B . In models M2 and M3 the jet variability is quite evident by the presence of a thin Mach disk in several internal working surfaces. In contrast, the map corresponding to model M4 and M5 have a more complex morphology with less defined working surfaces, and a larger cocoon structure due to the magnetic field along the symmetry axis.

3.2. Radio polarization study

Figure 3 shows synthetic maps of the intensity of the linearly polarized radio emission I_P , degree of polarization ($= I_P(\nu)/I(\nu)$, where $I(\nu) = \int i(\nu) ds$) thermal X-ray emission, and the distribution of the position angle of B . These maps were obtained considering that the jet axis is tilted 15° with respect to the plane of the sky.

¹The cooling distance (see e.g. the equation (6) of [Raga et al. 2002](#)) results larger than the jet radius, implying an adiabatic nature for the internal shocks.

In model M1 ($\Delta v = 0$) the jet develops a single radio knot associated with gas of the Mach disk (see Figure 3, top panels). Instead, the other models ($\Delta v \neq 0$) display knotty radio structures produced by the internal shocks². Model M4 ($B_z = B_m$) also shows radio emission in the region behind the main bow shock. The radio emission of this region in model M5 results lower than the emission in model M4, because of the longitudinal component of the magnetic field in model M5 is $B_z = B_m/3$ (see Table 1).

The X-ray emission maps also display a knotty structure although less defined than its radio counterpart. Most of the thermal X-ray emission comes from the environment material swept up by the main bow shock, as shown by Bonito et al. (2004, 2007, 2010) in hydrodynamic simulations.

In Figure 3 the degree of polarization of the synchrotron radiation shows an important result. Models M1-M3 exhibit a high degree of polarization of the synchrotron emission while model M4 displays a decrease toward the symmetry axis, mainly in radio knots at 3.75×10^{17} cm and 9×10^{17} cm from the jet source (this behavior is also observed in model M5, although to a lesser degree). These results can be understood considering that, in an helical magnetic field, emission from regions with linearly polarized synchrotron radiation whose polarization directions result orthogonal to each other cancel out when the emission is integrated along a LoS, which is nearly perpendicular to the axis of symmetry of jet. A decrease of the degree of polarization has been observed in the jet associated with HH 80-81 (Carrasco-González et al. 2010).

Maps of the distribution of the position angle of the magnetic field display a magnetic field parallel or perpendicular to the symmetry axis for model M4 and M5, while models M1-M3 mainly display a magnetic field perpendicular to this axis (see Figure 3).

4. Discussion and Conclusions

Carrasco-González et al. (2010) have shown the

²We are considering a jet with a fixed axis, and thus the working surfaces move along the axis of symmetry of the jet and never exit the cocoon carved by the main bow shock. Thus, their interaction is with the jet material and not with the external medium.

existence of polarized radio emission associated with the HH 80-81 protostellar jet. However, this issue has not been studied by HD or MHD simulations. We present the results obtained from 2.5 MHD simulations of an adiabatic and low-density YSO jet. We have considered cases with a constant and a time-dependent jet ejection velocity. Furthermore, cases in which the magnetic field is toroidal or helical were analyzed.

Assuming a population of relativistic electrons which are accelerated in stellar shock jets, we have used standard prescriptions to compute their synchrotron emission. Our results show that while the thermal X-ray emission is dominated by the shocked environment material located at the head of the jet (in agreement with Raga et al. 2002; Bonito et al. 2004, 2007, 2010), the non-thermal radio emission turns out to be dominated by the jet material at internal shocks.

Also, radio maps show that the variability in jet velocity is important in generating bright knots of synchrotron emission, produced when slow jet material is caught up by faster jet material.

Our models show that a jet with toroidal magnetic field emits synchrotron radiation with a high degree of polarization. Instead, models with a helical magnetic field exhibit a decrease on the degree of polarization, in good agreement with observational results (Carrasco-González et al. 2010).

MC, PFV, FdC, and AE thank financial support from CONACyT grants 167611 and 167625, CONICET-CONACyT grant CAR 190489, and DGAPA-PAPIIT (UNAM) grants IG 100214, IA 103115, IA 109715, IA 103315. A.T.A. acknowledges support from the UK Science and Technology Facilities Council under grant number ST/K00106X/1. C.C-G. acknowledges support by DGAPA-PAPIIT (UNAM) grant number IA 101214. LFR acknowledges support from CONACyT and DGAPA-PAPIIT (UNAM) grants. We also thank Enrique Palacios for maintaining the Linux Server on which the simulations were carried out.

REFERENCES

Blandford, R. D., & Payne, D. G. 1982, MNRAS, 199, 883

- Bocchino, F., Orlando, S., Miceli, M., & Petruk, O. 2011, *A&A*, 531, A129
- Bonito, R., Orlando, S., Miceli, M., Eisloffel, J., Peres, G., & Favata, F. 2010, *A&A*, 517, A68
- Bonito, R., Orlando, S., Peres, G., Favata, F., & Rosner, R. 2004, *A&A*, 424, L1
- . 2007, *A&A*, 462, 645
- Carrasco-González, C., Rodríguez, L. F., Anglada, G., Martí, J., Torrelles, J. M., & Osorio, M. 2010, *Science*, 330, 1209
- Clarke, D. A., Burns, J. O., & Norman, M. L. 1989, *ApJ*, 342, 700
- De Colle, F., & Raga, A. C. 2006, *A&A*, 449, 1061
- De Colle, F., Raga, A. C., & Esquivel, A. 2008, *ApJ*, 689, 302
- De Colle, F., Ramirez-Ruiz, E., Granot, J., & Lopez-Camara, D. 2012, *ApJ*, 751, 57
- Dere, K. P., Landi, E., Mason, H. E., Fossi, B. C. M., & Young, P. R. 1998, in *Astronomical Society of the Pacific Conference Series*, Vol. 143, *The Scientific Impact of the Goddard High Resolution Spectrograph*, ed. J. C. Brandt, T. B. Ake, & C. C. Petersen, 390
- Garay, G., Brooks, K. J., Mardones, D., & Norris, R. P. 2003, *ApJ*, 587, 739
- Garay, G., Ramirez, S., Rodriguez, L. F., Curiel, S., & Torrelles, J. M. 1996, *ApJ*, 459, 193
- Ginzburg, V. L., & Syrovatskii, S. I. 1965, *ARA&A*, 3, 297
- Gómez, J. L., Marscher, A. P., Jorstad, S. G., Agudo, I., & Roca-Sogorb, M. 2008, *ApJ*, 681, L69
- Jun, B.-I., & Norman, M. L. 1996, *ApJ*, 472, 245
- Laing, R. A., Canvin, J. R., Bridle, A. H., & Hardcastle, M. J. 2006, *MNRAS*, 372, 510
- Lind, K. R., Payne, D. G., Meier, D. L., & Blandford, R. D. 1989, *ApJ*, 344, 89
- Marti, J., Rodriguez, L. F., & Reipurth, B. 1995, *ApJ*, 449, 184
- Masciadri, E., Velázquez, P. F., Raga, A. C., Cantó, J., & Noriega-Crespo, A. 2002, *ApJ*, 573, 260
- Orlando, S., Bocchino, F., Reale, F., Peres, G., & Petruk, O. 2007, *A&A*, 470, 927
- Petruk, O., Dubner, G., Castelletti, G., Bocchino, F., Iakubovskiy, D., Kirsch, M. G. F., Miceli, M., Orlando, S., & Tezhinsky, I. 2009, *MNRAS*, 393, 1034
- Raga, A., & Noriega-Crespo, A. 1998, *AJ*, 116, 2943
- Raga, A. C., Noriega-Crespo, A., & Velázquez, P. F. 2002, *ApJ*, 576, L149
- Rodriguez, L. F., Curiel, S., Moran, J. M., Mirabel, I. F., Roth, M., & Garay, G. 1989, *ApJ*, 346, L85
- Schneider, E. M., Velázquez, P. F., Reynoso, E. M., Esquivel, A., & De Colle, F. 2015, *MNRAS*, 449, 88
- Tregillis, I. L., Jones, T. W., & Ryu, D. 2001, *ApJ*, 557, 475
- Wilner, D. J., Reid, M. J., & Menten, K. M. 1999, *ApJ*, 513, 775

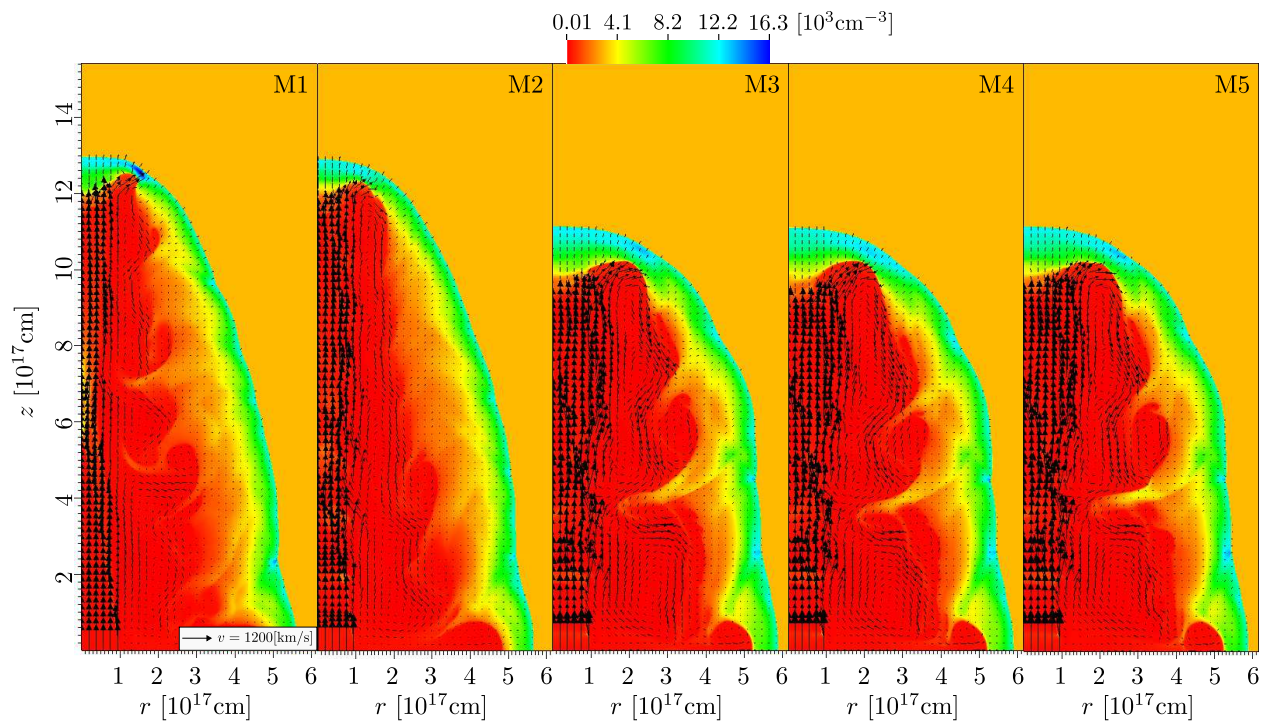


Fig. 1.— Number density stratification maps, in units of 10^3 cm^{-3} , and displayed in linear color scale. The integration time is $t = 1500 \text{ yr}$ in all models. The black arrows depict the velocity field (in units of km s^{-1}).

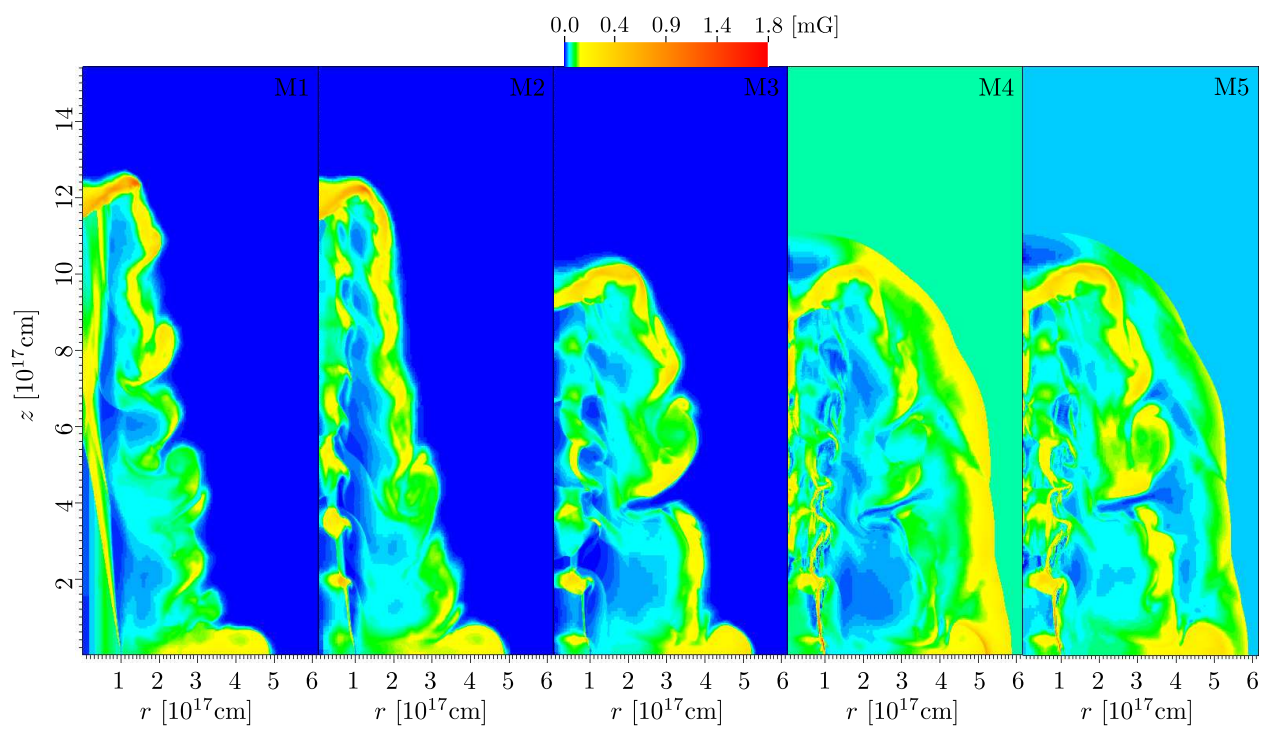


Fig. 2.— Maps of the total magnetic field intensity, (in units of mG) obtained for all models at an integration time of 1500 yr.

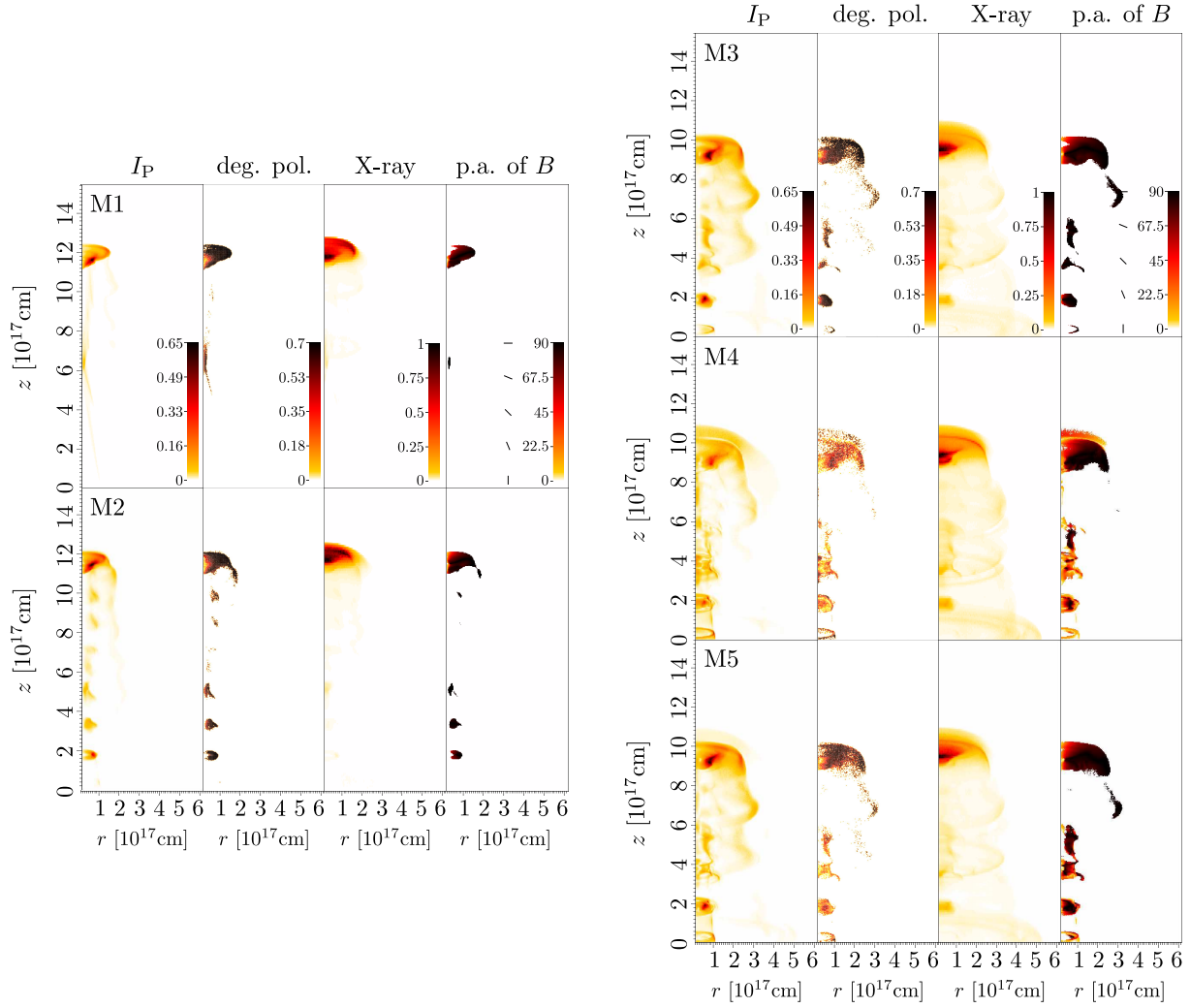


Fig. 3.— Left to right: synthetic maps of the intensity of the linearly polarized radio emission, degree of polarization, thermal X-ray emission, and position angle distribution of B (which is measured with respect to the z - axis, and whose orientation is represented by the stick marks). Top to bottom: M1-M5 models.